

Orientation dependence of plastic deformation in nickel-based single crystal superalloys: Discrete–continuous model simulations

A. Vattré^a, B. Devincre^{b,*}, A. Roos^a

^a DMSM, ONERA, 29 Avenue de la Division Leclerc, BP 72, 92322 Châtillon Cedex, France

^b LEM, CNRS-ONERA, 29 Avenue de la Division Leclerc, BP 72, 92322 Châtillon Cedex, France

Received 2 September 2009; received in revised form 20 November 2009; accepted 21 November 2009

Available online 21 December 2009

Abstract

The anisotropic mechanical response of single-crystal nickel-based superalloys is simulated. At 1123 K, two uniaxial tensile loading cases are simulated: one along [001] and another along [111]. Resulting stress–strain curves, stress distributions, interfacial dislocation structures are analysed. In accordance with experiments, the simulations show an anisotropic yield strength. The applied strain is accommodated by dislocations propagating through matrix channels on octahedral slip systems. The net result appears as slip bands along the cubic directions, even though no cubic slip systems are activated. In the [001] case, the plastic flow is distributed more or less evenly among the three matrix channels, whereas in the [111] case it is mainly concentrated in one single channel. Typical zig–zag configurations are observed. The elementary mechanisms controlling their formation are explained. Cross-slip does not play any role there. The hardening anisotropy between both loading cases is related to strong differences between the interfacial dislocation microstructures.

© 2009 Acta Materialia Inc. Published by Elsevier Ltd. All rights reserved.

Keywords: Nickel alloys; High-temperature deformation; Plastic deformation; Dislocation dynamics; Work-hardening modelling

1. Introduction

Single crystals of nickel-based superalloys are specifically developed for high-temperature applications [1,2]. These materials are used for turbine blades in aircraft engines and in power plants. Their particular microstructure consists of ordered γ' Ni₃Al precipitates with a L1₂ structure, coherently set in the γ -matrix, a face-centred cubic (fcc) nickel-based solid solution. Nickel-based superalloys derive much of their excellent mechanical properties at high temperature from the γ' precipitates. They have a roughly cuboidal shape and are regularly distributed, with faces parallel to the {100} planes and with narrow γ -matrix channels between them. The dimensions of precipitates and channels are in the sub-micrometer range. The trend in nickel-based superalloy development has been towards increasing their volume fraction up to values providing an optimum of mechanical properties: the first generation,

such as Waspalloy, contains about 25 vol.%, whereas more recently developed alloys contain up to 70 vol.%.

In uniaxial tension or compression tests, the yield strength depends strongly on loading direction and temperature [3–10]. For instance, at 1273 K and at low tensile stress, plasticity is mainly concentrated within the channels on $\frac{1}{2}\langle 110 \rangle\{111\}$ planes [11,12]. The precipitates are not plastically deformed, because of the anomalous yield behaviour of the Ni₃Al phase, whose flow stress increases from room temperature up to a peak value at about 1243 K [13]. Also, in the ⟨001⟩ loading cases (i.e. for crystals with one of the ⟨001⟩ axes oriented along the loading direction), the 0.2% yield stress and the strain hardening are considerably higher than for other orientations. Understanding such plastic behaviour is essential because the crystallographic alignment during blade solidification can deviate from the strongest ⟨001⟩ orientation, and blades can be subjected locally to complex stress states.

The question has been raised whether cube slip occurs in crystals oriented away from the ⟨001⟩ directions [6,7,9]. In

* Corresponding author. Tel.: +33 1 46 734155.

E-mail address: benoit.devincre@onera.fr (B. Devincre).

the $\langle 111 \rangle$ loading cases, i.e. for crystals oriented with one of the $\langle 111 \rangle$ axes along the loading direction, $\{100\}$ slip traces have been observed within the channels. Activation of cube slip systems has important consequences for the models of the orientation-dependence of the mechanical response [14–19]. Adopting cube slip is a convenient scheme to account for the softer plastic response of non- $\langle 001 \rangle$ oriented specimens. Microscopically, dislocations would then glide on the cubic planes in the matrix channels. The boundaries of those channels are parallel to the glide planes, so they cannot block these dislocations who could then glide freely over large distances.

However, at higher magnifications no dislocations were found to glide on cube planes [3,4,10]. Recent transmission electron microscopy (TEM) analyses [9,10,20] showed that the $\{100\}$ traces previously observed with optical microscopy consist of repeated slip occurring on different $\{111\}$ planes within the γ channels, appearing visually as zig-zag configurations. According to Bettge and Österle [9] and Wang et al. [10], this is a result of successive dislocation cross-slip between the $\{111\}$ slip planes. The cubic slip systems in the crystallographic viscoplastic models dedicated to single-crystal superalloys can then be thought of as phenomenologically representing the “pseudo-cubic” slip traces caused by the zig-zag slip on octahedral planes.

This paper seeks to clarify some of these issues by using three-dimensional dislocation dynamics (DD) simulations. Uniaxial tensile tests of a single crystal nickel-based superalloy are simulated at 1123 K, for a $[001]$ and for a $[111]$ loading case. The mechanical problem is solved through a coupled approach involving a DD and a finite element (FE) code, called the discrete-continuous model (DCM) [21–23].

The structure of this paper is as follows. First, the DCM is briefly recalled in Section 2. Then, the simulation results are given in Section 3. They aim at understanding the orientation dependence observed in the tensile tests. Calculations are then compared with the experimental results from the literature. The simulated dislocation microstructures and the internal stress distributions are analysed in detail in Section 4, providing original information on the dislocation mechanisms controlling plastic deformation in these tests. The simulations are shown to deliver a qualitative and quantitative description of plastic strain localisation, consistent with experimental observations.

2. Simulation method

2.1. The discrete-continuous model (DCM)

In the DCM, which is used throughout this paper, the usual constitutive law of a FE code is replaced by a discretized representation of the dislocation lines, as usual in a dedicated DD code. With this hybrid numerical approach the mechanical boundary problem and the associated physical processes can be solved simultaneously. On the one hand, the DD code (*microMegas* [22,25]) solves the dynam-

ics and the local reactions of discrete dislocation lines, and computes the plastic shear strain increments generated by dislocation glide. On the other hand, the FE code (*ZéBuIoN* [26]) computes the associated stress and displacement fields, the solution of the boundary value problem, using the plastic strain field given by the DD code. The DCM has already been used to study plastic relaxation in heteroepitaxial thin films [27], plastic deformation in metal matrix composites [28] and compression tests in a micro-pillar of Cu [29]. For details on the DCM the reader is referred to Refs. [21,30,31] and for the more recent developments of the numerical method to Ref. [23]. With these latest developments, the size effect of the channel width on the mechanical response of single-crystal γ/γ' superalloys has been analysed in a previous paper [32].

The simulated volume is periodic and contains only one γ' cuboidal precipitate surrounded by six γ channels. This volume is discretized by $16 \times 16 \times 16 = 4096$ quadratic finite elements and 56,361 degrees of freedom, with periodic boundary conditions (PBC). In order to avoid PBC artifacts due to self-annihilation of dislocation loops [33], the ideal periodic arrangement of cubic precipitates is modified by considering precipitates with orthorhombic dimensions ($0.48 \times 0.50 \times 0.52 \mu\text{m}^3$). At channel width $h = 0.08 \mu\text{m}$, the precipitate volume fraction becomes $f = 61\%$. Fig. 1a shows the simulated volume and some of its periodic replicas. For better visibility of the dislocation lines, not all of the precipitates are shown.

In *microMegas*, the dislocation lines are discretized into segments of screw, edge and two mixed characters (here $\pm 60^\circ$ character in the $\langle 110 \rangle$ directions). This discretization is numerically very efficient for the specific case of the γ/γ' superalloy, because dislocation-dislocation junctions between octahedral slip systems and dislocation segments arrested by the $\{100\}$ precipitate/matrix interfaces are all along $\langle 110 \rangle$ directions. This last point is illustrated in Fig. 1. Fig. 1a shows a dislocation (highlighted by a somewhat thicker line) gliding through the matrix channels on a $\frac{1}{2}\langle 110 \rangle\{\bar{1}11\}$ plane. The dislocation leaves behind dislocation segments pressed against the interfaces which have either a screw character in the horizontal channel (indicated by the black arrow in Fig. 1b), or a mixed character in the vertical channels, with a Burgers vector at $\pm 60^\circ$ with respect to the line direction (indicated by the black arrows in Fig. 1c).

For simplicity, isotropic elasticity is assumed everywhere with a shear modulus $\mu = 51 \text{ GPa}$ and a Poisson ratio $\nu = 0.37$. In the DD code, the lattice parameter $a = 0.36 \text{ nm}$ is assumed identical in both phases. This implies a Burgers vector of length $b \approx 0.25 \text{ nm}$.

Shearing of the precipitates has been incorporated into the DCM [34] and it correctly reproduces the anomalous temperature dependence [13] of the simulated bowing-assisted cutting process. In the γ' phase the main parameter controlling the dynamics of precipitate shearing is a configuration stress τ_{APB} , which accounts for an anti-phase boundary (APB) creation or recovery through the APB

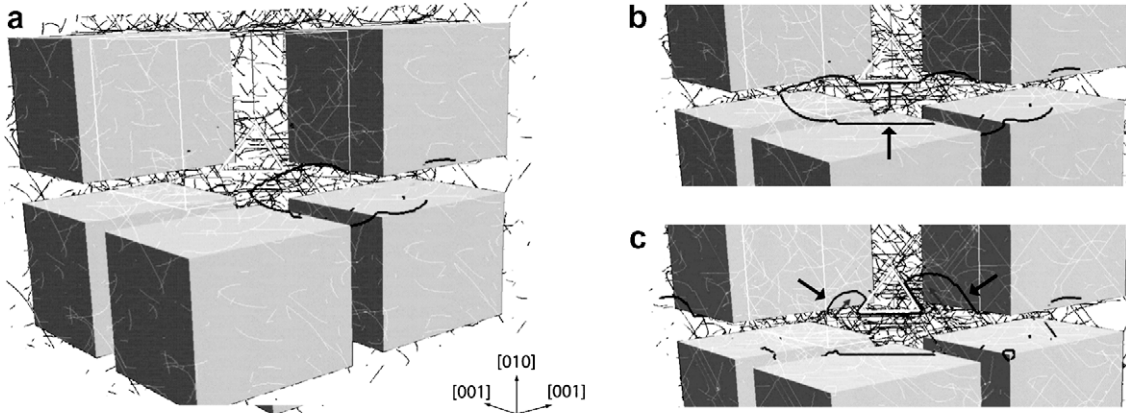


Fig. 1. (a) The simulated γ/γ' microstructure and some of its periodic replicas. The three possible types of dislocation character (screw and $\pm 60^\circ$ character) arrested by $\{100\}$ precipitate/matrix interfaces during the Orowan bypassing process are illustrated: in (b), the black arrow shows the screw segment deposited at the horizontal interface, whereas in (c), $\pm 60^\circ$ character segments are deposited at the vertical interfaces.

energy γ^{APB} . In all simulations of the present study, $\gamma^{\text{APB}} = 350 \text{ mJ m}^{-2}$ [35] and at 1123 K the precipitates are bypassed by the Orowan mechanism, i.e. the precipitates are only deformed elastically. This is consistent with experimental observations at small plastic deformations [11,12,36], where the dislocation loops move through the channels, bowing out between the precipitates when a critical shear stress, the Orowan threshold stress $\tau^{OR} \approx \mu b/h$, is reached.

In the γ phase, the velocity v of the dislocation segments is supposed to be linearly proportional to the resolved shear stress τ through $v = \tau b/B$. The viscous drag constant $B = 1.0 \times 10^{-4} \text{ Pa s}$ accounts for dissipative processes associated to dislocation motion. A constant lattice friction τ_F opposing dislocation motion due to solid-solution strengthening is subtracted from τ before calculating the segment velocity. Post mortem and in situ TEM observations on single phase crystals suggest the value $\tau_F = 105 \text{ MPa}$ [37].

2.2. Initial dislocation configurations

Initial conditions in DCM simulations should be as close as possible to the experimental conditions in terms of dislocation density, dislocation source distribution and dislocation entanglement. As explained in Refs. [23,31], the initial configuration in a DCM simulation is generated with a Volterra shearing procedure. This procedure is needed to set up an eigenstrain distribution [38] in the FE mesh that is mechanically compatible with the initial dislocation microstructure.

For reasons of simplicity and in order to avoid significant annihilation of dislocations in the first steps of the simulations, the initial dislocation distribution consists only of dipolar loops (four connected edge segments with the same Burgers vector). In this manner, dislocation segments act as Franck–Read sources and build up an interconnected dislocation network free of any pending lines.

A total dislocation density is homogeneously assigned to the 12 octahedral slip systems in the form of 24 dipolar loops. The slip systems are labeled according to the Schmid and Boas notation and cube slip systems are excluded on purpose.

The initial length of the edge segments is $0.12 \mu\text{m}$, which is longer than the channel width $h = 0.08 \mu\text{m}$. This precaution is needed in order to prevent artifacts due to a source activation stress operating within the γ channel which may be superior to the Orowan threshold stress. It has been verified that considering smaller initial dislocation source length than the channel width generates unrealistic macroscopic mechanical behaviour, which may include an initial overstress of several hundred megapascals. Indeed, dislocation segments can bow out and multiply at a simulated critical resolved shear stress ($\approx 113 \text{ MPa}$), which is lower than the theoretical Orowan stress of 163 MPa for this channel width. In order to assure the condition that each initial segment has a length of $0.12 \mu\text{m}$, the starting dipolar loops cannot lie exclusively in the channel: parts of the loops are located in the channel and other parts in the precipitate. The latter dislocation segments create an APB, so they are energetically unfavorable and the dislocation distribution must be relaxed before applying mechanical loading.

An additional strengthening mechanism is due to the lattice mismatch between the two phases. The difference in lattice parameter between the γ and γ' phases creates a coherency stress field, which is not well known experimentally at high temperatures [12,39]. In the DCM simulations, it can be computed by means of a preliminary thermoelastic FE calculation, by artificially heating the γ/γ' microstructure from an initial state without misfit at room temperature. This requires two thermal expansion coefficients, α^γ and $\alpha^{\gamma'}$, associated respectively to the γ matrix and γ' precipitate, and the appropriate heating interval ΔT . The misfit strain δ is then given by $(\alpha^{\gamma'} - \alpha^\gamma)\Delta T$, here equal to -3% at 1123 K. Fig. 2a shows the von Mises equivalent stress σ_{mises} of the coherency stress field in the

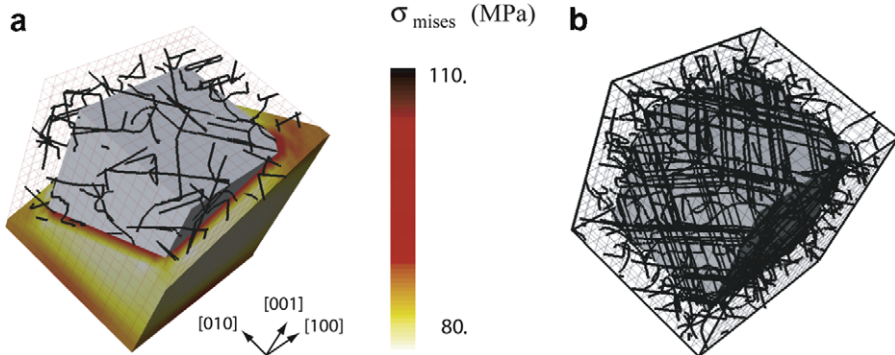


Fig. 2. (a) An initial dislocation configuration after relaxation. The persistence of coherency stress is illustrated by the von Mises stress σ_{mises} at the surface of a diagonal cut through the channels. This can be compared to the large network of dislocations found at the γ/γ' interfaces in (b), after 0.2% plastic strain for the [001] case.

matrix, before any mechanical loading. The matrix is in tension and the equivalent stress attains a minimum in the middle of the channels, and a maximum along the interfaces. In the precipitate, the misfit generates an uniform von Mises stress of about 30 MPa.

During the initial relaxation, the APB energy and the coherency stress drive the dislocations towards the interfaces. At this stage, the DD simulation time step is 5×10^{-11} s and the FE time step is 10 times as long. The dislocation configuration is supposed to be relaxed when there are no more dislocations inside the precipitate. Complete relaxation takes about 3000 DD steps. After the process, the total dislocation density on the 12 octahedral slip systems is $6.2 \times 10^{13} \text{ m}^{-2}$. As shown in Fig. 2a, the dislocations have moved to the interfaces, where they locally reduce the coherency stress.

It was observed that the relaxed configuration is modified even when a very small load is applied during the relaxation. For that reason, the configurations subsequently used for mechanical loading were obtained by imposing a tiny fraction ($\approx 10^{-7}$) of the mechanical loading that will be applied later on. This simple trick helps to eliminate possible transitory plastic deformation at the beginning of the simulation of the tensile test. It was verified that this modification does not change the mechanical response beyond this initial transitory stage.

Finally, not all initial configurations need the same time to eliminate their dislocation segments from the precipitate and to form the dislocation network at the interfaces. Those initial configurations which happen to have only a small fraction of segments inside the precipitate would probably need less time to relax than other initial configurations with almost all segments there. Therefore, in order to minimize the relaxation time, the dipolar loops are positioned in such a way that the fraction of their segments inside the precipitate is as low as possible. If the main concern of the present paper would have been the relaxation process itself, this procedure would of course not be justified, but here the interest is the dislocation dynamics and the dislocation–precipitate interactions during the subsequent mechanical loading.

Fig. 2a shows a relaxed dislocation configuration and the remaining coherency stress field just before mechanical loading. Fig. 2b shows the dense interfacial network after 0.2% plastic strain in the [001] case.

2.3. Loading conditions

During the simulations, the relaxed dislocation configurations are subjected to a pure tensile loading along the [001] or [111] axes. In order to run calculations within a reasonable time, a high resolved strain rate of $\dot{\gamma} = 20 \text{ s}^{-1}$ is imposed. Note that the convention is adopted throughout this paper that all macroscopic stresses or strains are resolved on the slip system(s) with the highest Schmid factor, unless specifically indicated otherwise. This strain rate is larger than the macroscopic strain rates applied in laboratory tests, but reducing it would not affect the conclusions of this work. Processes controlled by diffusion such as dislocation climb are not taken into account. Furthermore, cross-slip is not activated initially, but in a second set of computations a cross-slip process is taken into account for comparison with the pure glide results and for testing a hypothesis from the literature. The remaining simulation parameters are the same as during the plastic relaxation. However, contrarily to the relaxation phase, there is no longer any plasticity in the precipitates because at high temperatures plastic deformation takes place only through dislocation glide in the channels and the interfaces are effectively impenetrable [11,12]. Therefore, only a small fraction of the simulated volume is deformed plastically and a significant strain incompatibility is expected.

3. Simulation results

3.1. Macroscopic mechanical response

Fig. 3 shows the simulated stress–strain curves for both [001] and [111] cases. The two curves are in good agreement with experiments and are characteristic of plastic deformation of γ/γ' superalloys at high temperature

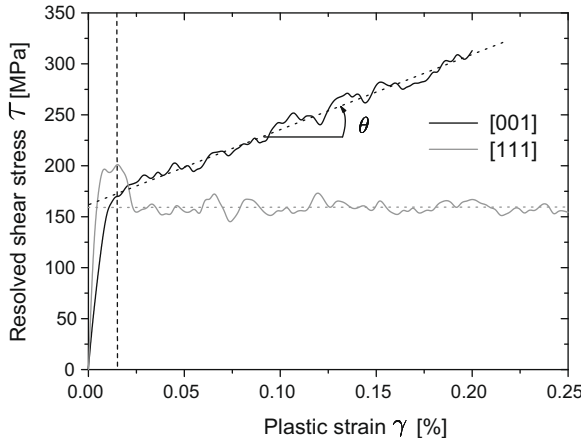


Fig. 3. Simulated stress–strain curves at 1123 K, in black for the [001] case and in gray for the [111] case. The dotted lines represent linear fits, except the vertical one, which indicates the boundary between the first and second stages.

[7,10,19]. Two distinct stages can be observed. During the first transient stage, from zero to 0.015% plastic strain, the flow stress is identical for both cases. The dislocations initially present in the channels start moving towards the interfaces. Due to the small channel width, the plastic deformation at 0.015% is mainly controlled by the line tension. The initial yield point correlates well with the Orowan stress prediction $\tau^{\text{or}} = k \mu b/h = 166 \text{ MPa}$ [40]. The prefactor $k = 1.02$ accounts for the mean character of the dislocation lines involved.

During the second stage (from 0.015% onwards), the relative influences of forest interactions or dislocation storage at the interfaces can increase potentially. In accordance with experiments, the two loading cases respond completely differently. The [001] case hardens linearly with slope $\theta = \Delta\tau/\Delta\gamma = 0.149 \mu$. The [111] case first shows a stress drop of about 50 MPa without any strain hardening afterwards. The form of this curve is typical: the experimental curves reported by Bettge and Co-workers [19] also show a stress drop of the same magnitude after an upper yield point, followed by a low-hardening domain. Moreover, the resolved flow stress calculated for both cases differ by approximately 130 MPa at 0.20% plastic strain. Again, this is in good agreement with experiments [19,41,42]: for instance, Österle et al. obtained a difference of 113 MPa at 923 K and 129 MPa at 1023 K for SC16 after 0.2% plastic strain at a strain rate of 10^{-3} s^{-1} .

In both loading cases, dislocation segments accumulate at the interfaces. Each dislocation gliding through a channel can deposit long, straight segments of opposite sign at the two opposite interfaces bounding the channel. At low effective stress, the deposited segments rearrange themselves on the interfaces in order to minimize the elastic energy. This creates the characteristic networks which have been observed many times in TEM studies [43].

Fig. 4 shows the evolution of the dislocation density ρ^{tot} with plastic strain. In conformity with the previous obser-

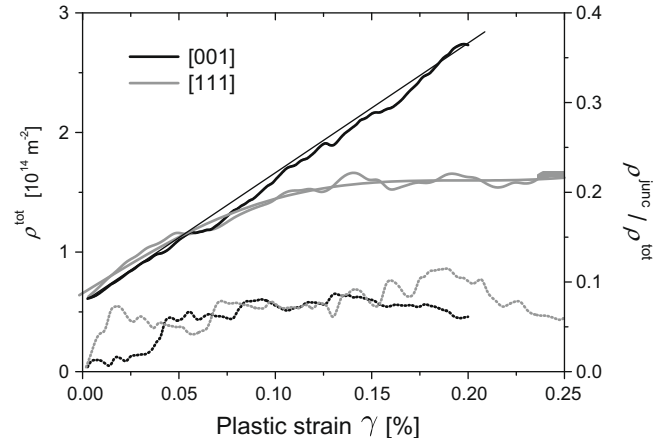


Fig. 4. Evolution of dislocation densities with plastic strain, in black for the [001] case and in gray for the [111] case. Solid lines: total dislocation density ρ^{tot} averaged over the whole simulated volume. Dotted lines: the ratio $\rho^{\text{junc}}/\rho^{\text{tot}}$ of junction density to total dislocation density.

vations on strain hardening, the net dislocation storage rate $\partial\rho/\partial\gamma$ is largest in the [001] case. Inversely, the absence of hardening for the [111] case manifests itself as a much lower dislocation storage. This results from plastic strain localization, but this will be explained in later sections.

The difference between the two cases is not caused by forest hardening. This is demonstrated in the same figure, where the ratio of junction density ρ^{junc} (which is a signature of forest hardening [44,45]) to total dislocation density is plotted as a function of plastic strain. The junction density is calculated here as the sum of the junction segment lengths divided by the simulated volume. For both cases, ρ^{junc} is much smaller than in usual fcc metals, and both ratios are quantitatively the same. Also, the rate of both ratios decreases after some straining. Even if all the junctions contributed to forest hardening, they would not contribute much to the flow stress in both loading cases.

3.2. Interfacial dislocation microstructures

Deformation incompatibilities between two phases can be accommodated by geometrically necessary dislocations accumulated at the interfaces [46]. These interfacial dislocations induce a long-range internal stress that contributes, with the applied stress and the coherency stress, to the total stress distribution in the microstructure. In the DCM simulations these contributions are calculated simultaneously, and a relation between mechanical strengthening and the dislocations stored at the interfaces is expected there.

Fig. 5 shows the dislocations deposited at the interfaces. Only those dislocations close to the interfaces (i.e. at distances smaller than 0.015 μm) are shown. For the [001] case in Fig. 5a, a dense network of straight dislocations is rapidly formed at all surfaces of the precipitate. This network consists of dislocations with four different Burgers vectors, homogeneously distributed between the three {100} interface directions. In the channel direction parallel

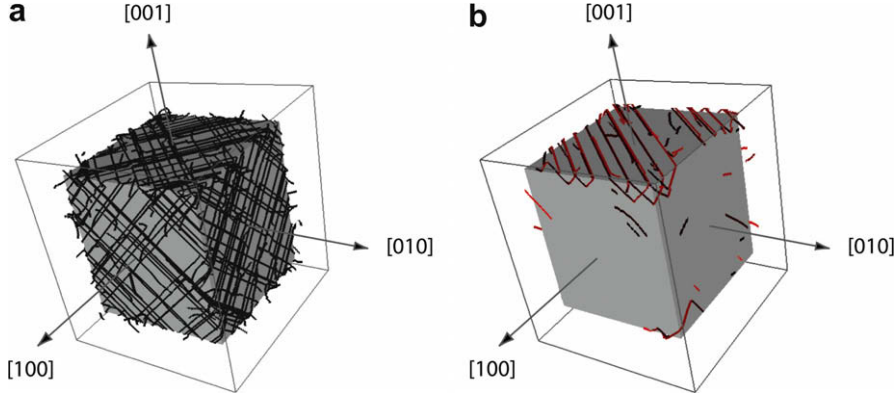


Fig. 5. Dislocation networks formed at the γ/γ' interfaces after deformation to 0.2% plastic strain. Only dislocations within a distance of $0.015 \mu\text{m}$ from the interfaces are shown for (a) the [001] case and (b) the [111] case.

to the loading axis, the line character of the interfacial dislocations is exclusively of $\pm 60^\circ$ type. In the two channel directions normal to the loading axis it can be either screw or $\pm 60^\circ$ type. This results from the direction of the Burgers vector of the activated slip systems.

In the [111] case (Fig. 5b), a completely different configuration is found. The dislocation network is restricted to only one interface direction. It consists of long parallel screw segments, all with the same Burgers vector ([110] in the figure). This configuration is one reason for the absence of hardening that was observed previously. Dislocations multiply in one single crystallographic direction and are confined to the channel containing this direction. The periodic arrangement of precipitates does not block the dislocation motion, and so it does not cause strain hardening either.

In Fig. 5b, positive dislocations gliding on A6 are indicated in red and negative dislocations gliding on D6 in black. The relative equilibrium and the homogeneous distribution of red and black colors at the interfaces indicate that the interfacial dislocations do not induce a long-range stress. This will be discussed further in Section 4.3.

The strong differences between these interfacial dislocation microstructures suggest a correlation with the hardening anisotropy. In order to clarify exactly what mechanisms affect the strain hardening, a more detailed analysis is presented in the next section.

3.3. Analysis of slip systems and deformation bands

Fig. 6 shows the plastic shear on each of the twelve octahedral slip systems. In accordance with the Schmid law, eight slip systems are found active in the [001] case. However, their contributions to the total plastic deformation are not distributed evenly. Several simulations were run in order to establish that this results from heterogeneities in the initial dislocation configuration. Activation of all eight slip systems is coherent with strong hardening and the dense dislocation microstructure found at the interfaces.

In the [111] case, six slip systems have identical non-zero Schmid factor. Surprisingly, only two slip systems

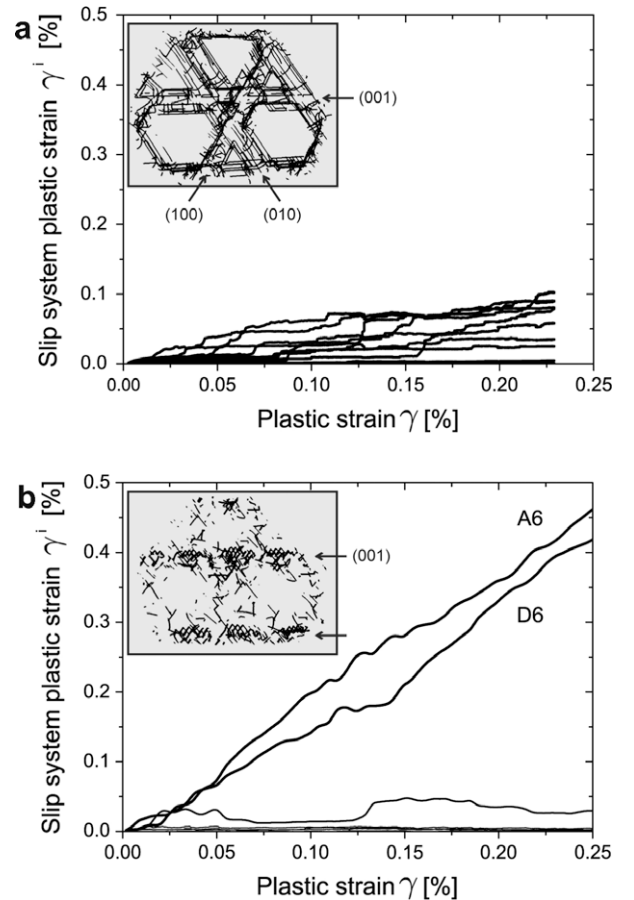


Fig. 6. Plastic strain γ^i on individual slip systems i . (a) In the [001] case, eight slip systems are activated more or less equally, in accordance with the Schmid law. (b) In the [111] case, only two slip systems are activated, whereas six slip systems have the same non-zero Schmid factor. Thin foils in the {111} direction are shown in the top left part of figures (a) and (b) in order to illustrate the relation between slip system activity and dislocation microstructure.

accommodate the imposed strain rate. For instance, in Fig. 6 the two active slip systems are A6 and its collinear system D6. The same duplex collinear slip is observed for four other initial dislocation microstructures. In each sim-

ulation the total plastic strain is accommodated by only two slip systems: one primary system (not necessarily the same for each initial microstructure) and its collinear slip system. These two particular slip systems are correlated because they always have the same Burgers vector. Duplex collinear slip has been referenced as the strongest existing forest interaction [47,48], so it should cause very high strengthening. However, the opposite is observed here. Clearly, the manner in which duplex collinear slip influences the mechanical response needs to be clarified in this particular case.

At high temperature, octahedral slip traces are very short because plastic deformation is confined to the channels, and deformation bands are observed parallel to the $\langle 100 \rangle$ directions. The deformation bands can be visualized by showing the dislocation lines stored in a thin slice of the channels. In the insets in Fig. 6 deformation bands are shown in slices of $0.15 \mu\text{m}$ thickness, with $[111]$ normal and at 0.20% plastic strain, extracted from the periodic simulation cell. At low magnification, plastic deformation indeed appears as slip bands parallel to $\{100\}$ cube planes. However, in the $[001]$ case (Fig. 6a) plastic strain is distributed more or less evenly among the three $\langle 100 \rangle$ directions, whereas in the $[111]$ case (Fig. 6b) the plastic deformation is restricted to only one direction.

It might be argued that the localization of the plastic deformation into one single channel in the $[111]$ case is caused by the lattice mismatch at the γ/γ' interfaces. However, this would create the opposite effect. This can be seen as follows. Without external loading, the mismatch creates a misfit stress, which is the same in each channel. Loading along a $\langle 111 \rangle$ direction would preserve this symmetry whereas loading along a $\langle 001 \rangle$ direction would not. If there was to be any localization because of the misfit stress, it would therefore be in the $[001]$ case, and not in the $[111]$ case. Moreover, simulations were carried out with two other coherency stresses ($\delta = -2\%$ and -3.5%), and it was observed that the internal stresses in the calculation do not affect either the macroscopic or the microscopic behaviour (it would have affected the initial dislocation configuration if the relaxation phase had been included, but that is not the case here). Rather, such a localization appears to be the result of an elementary dislocation reaction promoting dislocation glide in a specific direction and confining the deformation into one specific channel. The plastic strain remains localized throughout the whole loading path, so it must also be explained how this dynamical property is related to the absence of strain hardening in the $[111]$ case.

In summary, dislocation dynamics and dislocation storage depend strongly on the orientation of the channels relative to the tensile axis. In the $[001]$ case, the activation of several octahedral slip systems leads to the formation of deformation bands parallel to the $\{100\}$ directions. Plastic deformation in those bands is homogeneously distributed. Alternatively, the deformation bands in the $[111]$ case are systematically parallel to one unique cubic direction. This direction appears to be randomly selected in the early

stages of deformation. The selection depends on which particular glide systems succeed first at depositing the long screw dislocation segments at the interfaces, and this, in turn, depends on the random fluctuations between one initial configuration and another. Subsequent plastic deformation is then accommodated completely there. Additional work is needed to understand how such an instability is related to the duplex collinear slip observed in the $[111]$ case. The second part of this paper aims to identify dislocation reactions controlling this complex plastic behaviour.

4. Dislocation dynamics analysis

4.1. Pseudo-cubic slip

In one of the very few experimental studies addressing the occurrence of cube slip in γ/γ' alloys, Bettge and Co-workers [19] observed the appearance of slip bands by TEM. Single crystals oriented with the $[111]$ -direction near the tensile axis were deformed in uniaxial tension at 923 and 1023 K. The deformation bands appeared in two stages: at a low plastic strain of 0.20%, the first deformation bands were all parallel to one single cubic direction. Then, at a larger plastic strain of 2.55%, deformation bands were homogeneously distributed along all three $\{100\}$ directions. No cubic dislocations were observed at higher magnifications in both stages. The deformation bands contained only $\frac{1}{2}[011]\{111\}$ -type dislocations of mixed 60° character, forming zig-zag configurations in the matrix channels (Fig. 7). The angle between the zig and zag directions was approximately 60° . Note that the results from the DD simulations correspond to these observations for the first stage (see Fig. 7), albeit at a somewhat higher temperature.

According to Sass et al. [6,7] and Bettge and Österle [19], repeated double cross-slip events might explain the formation of the zig-zag configuration and the pseudo-cubic slip traces. Their explanation is as follows: a $\frac{1}{2}[011]$ screw segment gliding in a channel on a $(1\bar{1}\bar{1})$ plane will eventually be blocked by a (100) interface. As a result of some high local internal stress it cross-slips onto a $(1\bar{1}\bar{1})$ plane. After crossing the channel on this new plane, the segment is blocked again by the interface at the other side of the channel. There it cross-slips back onto a $(1\bar{1}\bar{1})$ plane. If this double cross-slip process occurs repeatedly, the initial screw segment generates two trailing zig-zag-shaped dislocations, tracing its path. Subsequently, the two trailing dislocations glide in the $[011]$ direction, thereby shearing the material with a net cubic (“pseudo-cubic”) slip.

In order to test this mechanism, two distinct sets of DD simulations were carried out. In the first set, the cross-slip mechanism was suppressed artificially, whereas in the second set it was not. Unfortunately, the way in which cross-slip actually occurs in γ/γ' superalloys is not known. Therefore, another constitutive rule for cross-slip had to be used, similar to the one used in pure fcc metals [49].

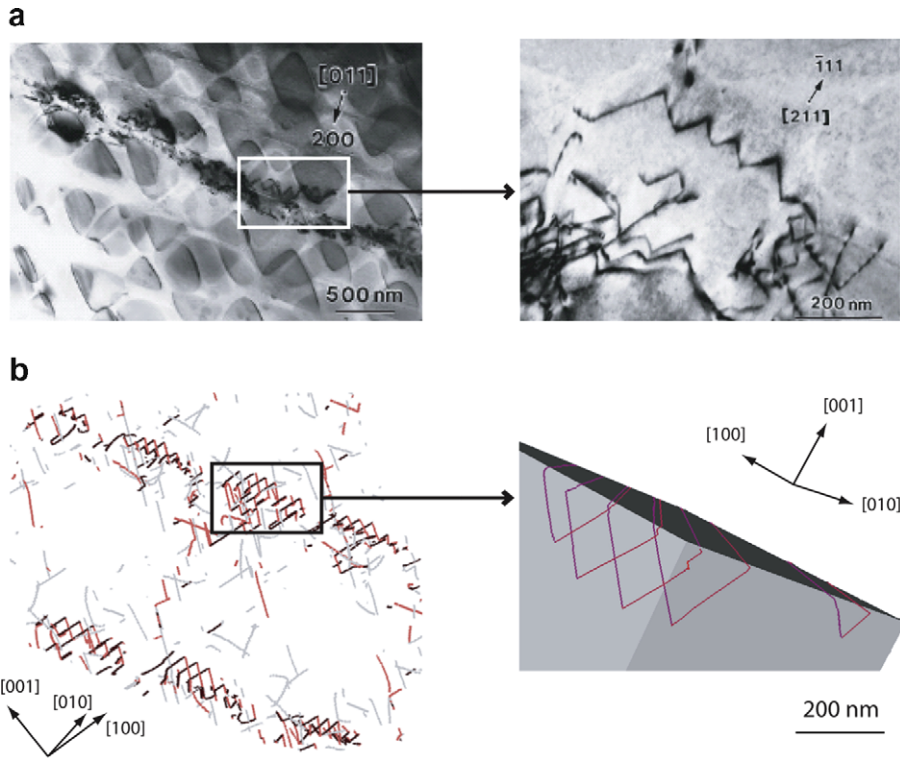


Fig. 7. Comparison between (a) experimentally observed (after [19]) and (b) simulated dislocation microstructure in a matrix channel for the [111] case, after 0.2% plastic strain. (a) Left: TEM bright-field image with foil normal (111) of a (100) slip band at 923 K. Right: enlarged view of the rectangular area in the image on the left showing zig-zag dislocation configurations. (b) Simulated dislocation microstructure at 1123 K with the same foil characteristics.

In both sets of simulations, exactly the same zig-zag configurations were obtained as in Fig. 7. Therefore, the formation of the zig-zag configuration is not necessarily associated to cross-slip, but rather must be the outcome of contact reactions during dislocation glide. In the next section, it is demonstrated that the simulated zig-zag configurations are the result of collinear annihilation [50] between dislocations with the same Burgers vector gliding in different slip planes.

4.2. Elementary mechanisms

The [111] case is analysed first. Only two slip systems with the same Burgers vector accommodate the imposed deformation. A simple analysis of dislocation-dislocation reactions shows that dislocations are either elastically repulsive or strongly attractive, and can annihilate upon contact in the collinear reaction [51]. In single-phase materials, this reaction can annihilate very long sections of the dislocation line. Therefore it has a significant impact on strain hardening and dislocation patterning [50,52]. In the specific case treated here, the contribution of the collinear reaction appears to be very different as a result of the confinement of the dislocation dynamics in the narrow channels. Consequently, the following points need clarification: (i) how the zig-zag configurations are formed; (ii) how collinear reactions cause the localization of the plastic deformation into a single cubic

direction; and (iii) why the [111] and the [001] cases are so different.

Fig. 8 shows the expansion of two dislocation loops on two different slip planes, but with the same Burgers vector. The snapshots are illustrations of the most frequently occurring collinear reaction during massive simulations (i.e. simulations where loops are present on all slip systems and with realistic dislocation densities). Because of line tension anisotropy, dislocation loops expand preferentially in those channels in which their edge segments can move large distances (in the figure this corresponds to the horizontal channel). Screw dislocation segments are deposited at the precipitate surfaces bounding these channels. Other screw segments cross the vertical channels but do not bow out there much because they are held back by the higher line tension in those directions. As illustrated in Fig. 8 at t_4 and t_5 , if the intersection of the two slip planes does not lie too far into the vertical channel, the screw line sections of both dislocations are annihilated there. This leaves behind "V"-shaped dislocation debris of 60° character against the two precipitate surfaces which bound the vertical channel. The accumulation of such "V"-shaped debris during plastic deformation is the explanation of the zig-zag configurations observed in the simulations (see Fig. 7).

As shown above, dislocations of a given Burgers vector preferentially glide in a specific channel because of the line tension anisotropy. Consequently, within the plastically

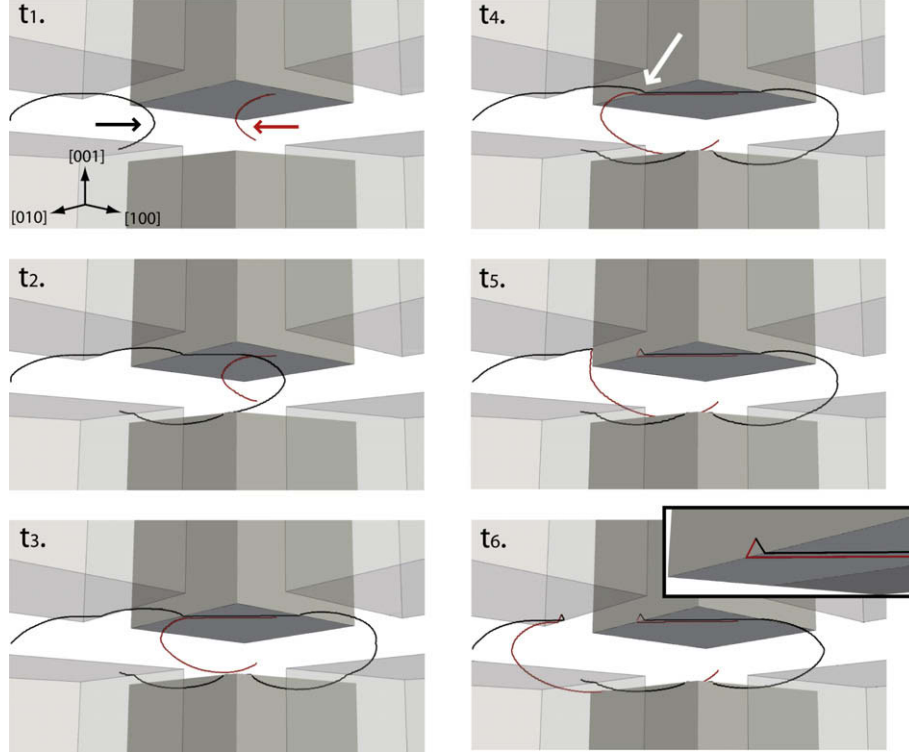


Fig. 8. Six successive stages t_1 – t_6 of the creation of “V”-shaped dislocation debris, the elementary parts of the zig-zag configuration. The two arrows at t_1 indicate the direction of movement of two dislocations with the same Burgers vector through the horizontal channel. The white arrow at t_4 points to the localization of the initiation of their collinear reaction in a vertical channel.

active channels there is a high probability of collinear interactions, and a large diversity of reactions is indeed observed there. Fig. 9 shows three representative examples.

Fig. 9a shows the simplest one. Two attractive dislocations bow out on intersecting planes, but now the planes intersect inside the active channel instead of outside, as in the previous case. The line of intersection is shown as the dotted line in Fig. 9a₃. The dislocations exchange line sections (“arms”) as a result of a collinear reaction, and again two “V”-shaped configurations are formed. This time, however, there are no vertical interfaces to block them, and they can glide across long distances after the reaction.

Fig. 9b shows subsequent possible reactions between “V” configurations (or even more complex dislocation configurations). For each collinear reaction an exchange of dislocation arms is observed, and the new dislocation configurations contain collinear superjogs, forcing dislocation glide in the direction of the Burgers vector. The latter direction is parallel to the channel interfaces, so the new dislocation configuration is potentially mobile. Two cases can now be distinguished: (i) the superjog glides in the same direction as the primary line. For the same applied stress the total force acting on the dislocation line then increases, because it is now longer than before. This facilitates cutting or bypassing obstacles, so that its mobility increases [50] (see Fig. 9b). (ii) The superjog glides in the opposite direction as the primary line. Then it tends to increase its length and bows out, and sometimes acts as a dislocation source (see Fig. 9c).

The larger the plastic deformation, the more collinear superjogs accumulate along the dislocations. This evolution justifies two important properties of the [111] case. First, the decoration with collinear superjogs enforces a localization of dislocation motion in their initial channel as they can glide easily only in the direction of the Burgers vector. Secondly, superjogs increase the mobility of some dislocations, because they increase the length of those mobile lines which can progress easily in between the interfaces.

The plastic localization observed in the simulations is certainly exaggerated because of the ideal arrangement of the periodic replicas of the precipitate. In reality, the precipitate arrangement is not perfectly regular and, because of that, the easy glide simulated here, with a very long dislocation free path, will eventually be blocked by some precipitate. At larger strains, additional slip systems must then be activated in the other channels.

Next, the [001] case is analysed. In this orientation we need to understand why the same elementary dislocation reactions do not lead to the same plastic instabilities as in the [111] case. At the start of the simulation of the [001] case the first slip systems activated in a channel are depositing pure screw segments at the γ/γ' interfaces, as in the previous case. Hence, the argument of line tension anisotropy promoting collinear duplex slip in specific channel directions also applies here. However, this time the plastic strain does not localize into one single channel, and a very

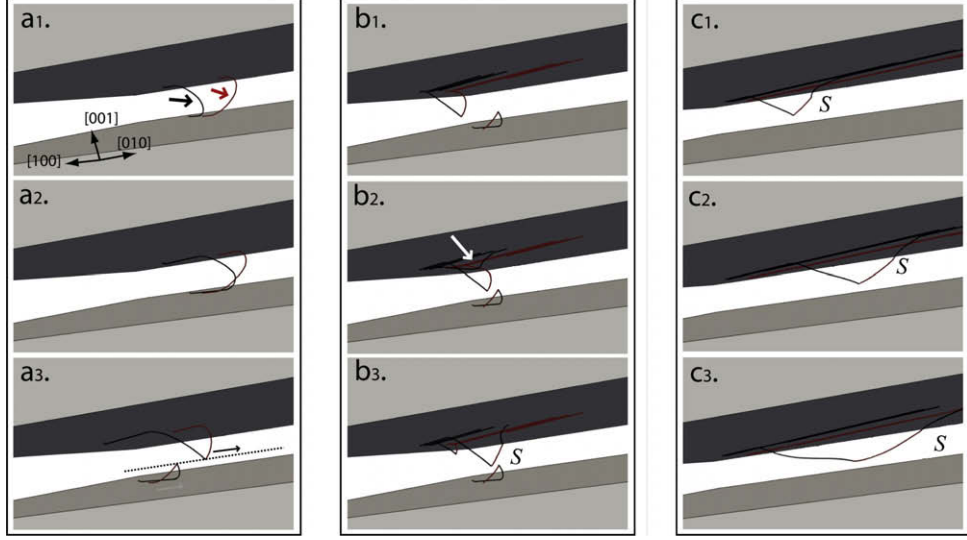


Fig. 9. (a) The collinear reaction: two curved dislocations with the same Burgers vector are gliding in a γ channel. After a collinear reaction, dislocation arms can only move in the same channel and in the same direction (illustrated by the dotted line and the black arrow at a_3). (b) Creation of a superjog S : mobile arms can react with an immobile dislocation to create a superjog (shown by the white arrow at b_2). The latter moves in the same direction as the primary lines, thereby increasing the mobility of the dislocation. (c) Creation of another superjog S : in this case it moves in the opposite direction as the primary lines, thereby increasing its line length. The newly created dislocation line can then bow out and even act as a dislocation source.

strong strain hardening is observed. The origin of this strain hardening is explained in the next section.

In agreement with other simulations on single-phase fcc crystals [50], the mobility of dislocation lines decorated with collinear superjogs is different between the two loading cases. As explained in Ref. [50], in the [001] case, most collinear superjogs decorating the dislocation lines are resistive. They tend to move in the direction opposite to the main line and must be dragged along by the mobile dislocations, thus increasing the flow stress somewhat. They also increase the rate of dislocation multiplication, because the long collinear superjogs can act as dislocation sources. This contributes significantly to the high strain hardening observed in the [001] case.

4.3. Strain hardening mechanism

In the previous section it was observed that the same dislocation reactions give very different plastic responses for the two loading directions. In the [111] case, dislocation mobility is high and there is no strain hardening. This is why the localization of plastic strain into one specific channel can hardly be stopped once it has been initiated. In the [001] case, dislocation mobility is lower, the multiplication rate is high and there is significant strain hardening. Given that forest hardening hardly contributes to the flow stress (see Section 3.1), the internal stress in the simulated volume is now analysed in order to identify the dislocation mechanisms that govern strain hardening.

A first hypothesis is that the strain hardening in the [001] case is an incidental effect of the larger number of slip systems that can be activated. To test this hypothesis, a model simulation containing only dislocation loops on

two collinear slip systems A6 and D6 was carried out for both loading cases. The resulting stress-strain curves are very similar to the ones obtained with loops on all slip systems. In addition, the evolution of the total dislocation density in these simulations has the same tendency as in Fig. 4. For the [001] case, interfacial dislocations are accumulated around all channels. For the [111] case, only a few screw dislocations are stored at the interfaces of one channel. This demonstrates that the observed strain hardening does not depend on the number of activated slip systems. Rather, it depends on the manner in which the dislocations are stored at the interfaces. In the simulations, this orientation dependence of the dislocation density distribution and the resulting hardening is obtained when at least two collinear slip systems are activated. The importance of the simultaneous activation of collinear slip systems is justified in what follows.

Next, returning to the massive simulations, the strain hardening of both orientations can be linked to the internal stresses created by the dislocations stored at the interfaces. Fig. 10 shows the internal stress τ^{int} in the simulated volume for both loading cases. This is calculated as the self-stress field of all dislocations resolved on one $(\bar{1}11)$ [110] active octahedral slip system in an infinite periodic microstructure. The images in Fig. 10 are the averages of ten cross-sections of normal [001], taken at regular intervals along the entire edge of the simulated volume.

From Fig. 10a, the strain hardening in the [001] case can be correlated to the high internal stress in the channels. Analysis of the dislocation dynamics in the active slip planes shows that the Peach-Köhler force on gliding dislocations is systematically reduced by the stress field of the dislocations accumulated at the interfaces. The origin of

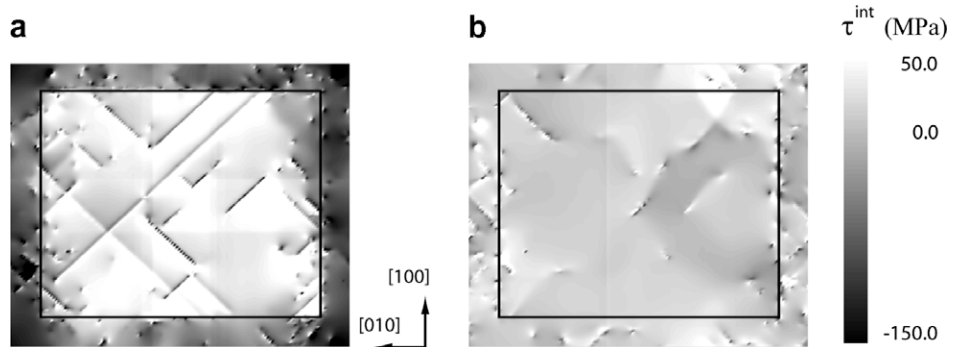


Fig. 10. The internal stress τ^{int} in the simulated γ/γ' microstructure for (a) the [001] case and (b) the [111] case.

this polarized internal stress is that the sign and amplitude of the Schmid factors on collinear slip systems are identical. As a consequence, the sign of the dislocations gliding in a crystal direction and the sign of the dislocations accumulated at a given interface are identical. In addition, with the elevated multiplication rate (see Section 4.2), the repulsive back stress associated to interfacial dislocation rapidly prevails. This explains why the dislocation dynamics is rapidly distributed among the three channels. Dislocations of screw and $\pm 60^\circ$ character are then found at the precipitate surfaces.

In the same manner, absence of strain hardening in the [111] case can be explained by two observations: (i) the interfacial dislocation network is not polarized; and (ii) the dislocation density during deformation remains low. The first point occurs because the Schmid factors on collinear slip systems are of opposite sign. For a specific line direction of the long screw segments covering a specific interface, the sign of the Burgers vector is not unique. As shown in Fig. 10b, this generates only a low internal stress in the microstructure which hardly contributes to the strain hardening. The second point is explained as follows: as a result of the many collinear reactions taking place inside the channel, a dislocation segment decorated with an odd number of collinear superjogs and which remains in the same channel is necessarily connected to two interfacial dislocations with identical signs (see Fig. 11). For such segments, the length of dislocation on different slip planes is unbalanced, so they can glide in the screw direction, but at a constant length of interfacial dislocations. These two points explain how the channels can be easily deformed plastically with hardly any increase in the dislocation density.

Lastly, it must be noted that the strain hardening is essentially kinematic in nature because it is mainly controlled by the formation of a polarized interfacial dislocation network. The internal stress in the channels created during a [001] tensile test would increase dislocation mobility in a subsequent compression test. More generally, one can conclude from the analysis of the simulated results that a strong kinematic hardening is expected in single-crystal superalloy samples deformed uniaxially in a direction close to one of the $\langle 001 \rangle$ directions. Also, a smaller

and more isotropic hardening is expected in uniaxial tests where the Schmid factors on collinear slip systems have opposite signs, e.g. with the tensile axis close to the $\langle 111 \rangle$ or $\langle 101 \rangle$ crystal directions.

5. Concluding remarks

Single-crystal superalloys with a high volume fraction of Ni_3Al γ' precipitates, regularly distributed within a matrix of solution-strengthened NiAl γ phase, have outstanding high-temperature mechanical properties, making them the designer's choice for turbine blades. The high-temperature strengthening of these single crystals has been the subject of numerous experimental and theoretical studies. The geometry and spatial arrangement of the γ' precipitates and the narrowness of the γ channels between them are known as the major factors contributing to their strength. For instance, the flow stress depends on the channel width. Furthermore, due to this particular arrangement, their mechanical response is very sensitive to the orientation of the crystal with respect to the external load. Experiments have shown that the flow stress is higher when loaded in uniaxial tension along the [001] direction than along [111].

Many studies have modelled this mechanical response by using the FE method. However, conventional continuum theory can predict neither the anisotropy nor the size dependence. Rather, they have to be included a priori, for instance by explicitly introducing a length scale into the constitutive descriptions, or by adding additional mechanisms to account for the anisotropy.

In this work, simulations have been carried out containing an intrinsic length scale, which is the length of the Burgers vector. The numerical discrete-continuous model solves the equilibrium and compatibility conditions under complex loading of a dislocated material containing interfaces. The objective of these simulations was to reproduce the macroscopic response for the [001] and [111] cases, and to analyse the resulting dislocation structures in order to understand the differences. Precautions have been taken to obtain realistic initial dislocation microstructures, and the dislocation analyses have been compared with experiments. The main results are summarized as follows:

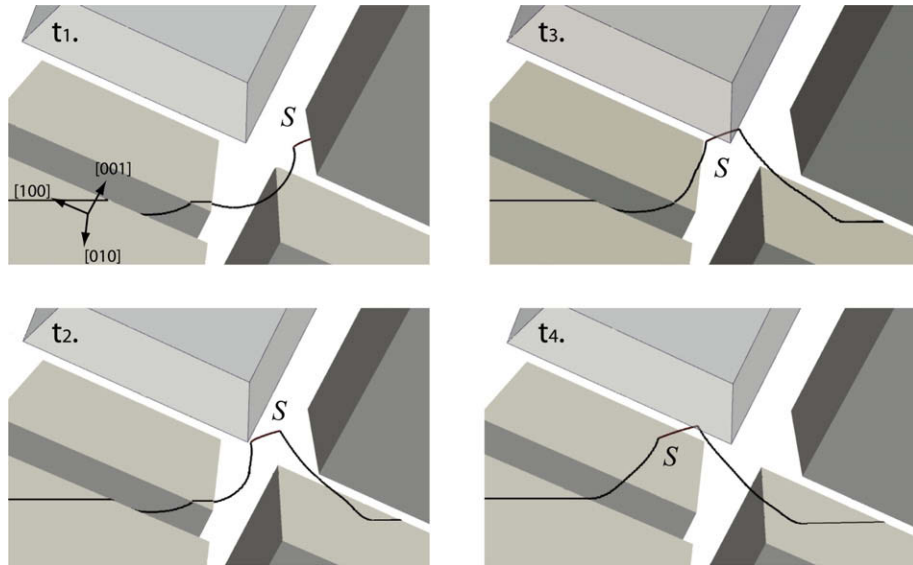


Fig. 11. Dynamics of a dislocation line decorated with a collinear superjog, moving in the screw direction. Glide of the line section in the γ channel (including the superjog S) produces plastic deformation, but without variation of the total dislocation length.

- In accordance with experiment, the macroscopic stress-strain curve for [001]-oriented specimens exhibits a strong linear hardening, whereas the stress-strain curve for the [111] orientation shows a stress drop after an upper yield point, followed by a low hardening stage. The difference has been correlated with much less dislocation storage for the [111] case than for the [001] case. In addition, at small strains forest hardening does not significantly influence the mechanical response because it is rendered ineffective by the dislocation–precipitate interaction.
- DCM simulations have shown that all dislocations are ultimately stored at the γ/γ' interfaces. When the Orowan stress is reached, dislocation loops move through the channels, bowing out between the precipitates and depositing dislocation segments at the interfaces. For the [001] case, these discrete segments have a screw character or a mixed 60° character, and the interfacial dislocation network thus created is polarized. For the [111] case, only two active octahedral glide systems deposit dislocation segments at the channel walls. These long parallel screw segments all have the same Burgers vector. Due to the fact that the two active systems are always collinear, the number of possible dislocation reactions is strongly reduced.
- Dislocation structures at the interfaces differ strongly between both orientations. In an optical microscope, the dislocation structures appear as deformation bands parallel to the $\{100\}$ cube planes. In the [001] case, eight octahedral slip systems are activated and a dislocation network is formed at all six surfaces of the precipitate. This appears as deformation bands along all three cubic directions. In the [111] case, the dislocation network is formed only on two interfaces, because the dislocation dynamics takes place only within one channel. In accor-

dance with experiment, the deformation band is located within one unique channel. This channel is deformed almost exclusively by only two slip systems.

- As previously observed experimentally by Bettge and Österle [9], at the fine scale, zig-zag dislocation configurations are observed. Such configurations are more easily observed in the [111] orientation because the dislocation density is lower there, but they exist whatever the loading axis. These zig-zag configurations are the product of collinear annihilation reactions between dislocations in slip systems having the same Burgers vector. Two kinds of zig-zag configurations are observed: (i) a series of immobile “V” debris located at the interfaces; and (ii) very mobile jerky dislocation lines decorated with collinear superjogs, confined within a channel. The latter are responsible for the localization of the plastic deformation and are the main mechanism for the easy glide observed in the [111]-oriented specimens.
- During the localization of the plastic deformation in the [111] orientation, long segments with the same Burgers vector but with opposite line vectors are deposited at the interfaces. These geometrical configurations are not polarized at interfaces and so do not create long-range internal stresses. In addition, the high mobility of superjogs within the deformed channel increases the possibility of annihilation of these long interfacial segments, thus explaining the reduction of the dislocation storage rate during deformation. Hence, the absence of hardening in the [111]-oriented specimens is caused by the diminishing evolution of dislocation density and the absence of long-range internal stress.

Guidelines to improve the constitutive laws for γ/γ' single crystal superalloys used in continuum modelling can be deduced from the simulations. Many crystal plasticity

models use additional cubic slip systems in order to capture the tensile anisotropy between the [001] and the [111] case phenomenologically. At a macroscopic scale this assumption is justified by the presence of deformation bands along the cubic directions. However, at lower length scales or (presumably) for more complex loading cases this is no longer valid. Moreover, such a simplification is not needed for large-scale computations:

- In the [001] case, the storage of dislocations into a polarized interfacial network can be modelled by considering the polar/excess/geometrically necessary dislocation density. Most of the dislocation density is concentrated at the interfaces instead of into pile-ups. It can then be supposed to be concentrated at a singular surface and be measured by the surface dislocation density tensor defined by Nye [53].
- Concerning the strain hardening, forest hardening can be neglected and only the long-range internal stresses generated through the Nye tensor should be taken into account. The expressions of internal stresses can be calculated by Green's functions or by Fourier series, because the microstructure can be approximated by an infinitely extended cuboidal microstructure.
- The anisotropy of the strain hardening is essentially determined by the nature of the dislocation network at the interfaces. For the [111] case, the interfacial dislocations are not geometrically necessary, in contrast to the [001] case discussed above. In order to capture this difference, the sign of the Burgers vector of each interfacial dislocation should be taken into account explicitly. One way to do this is to split the usual 12 octahedral systems containing dislocations of both signs into 24 systems containing dislocations of only one sign. Then, depending on the sign of the Schmid factor, one specific interfacial dislocation may have (for instance) a positive sign of the Burgers vector in the [001] case, whereas the same dislocation will have a negative sign in the [111] case [54]. The net effect is a different macroscopic response for the two cases.

The latter points have been taken into account in the enrichment of a dislocation density-based micromechanical model developed previously by Fedelich [16]. This will be published in a forthcoming paper [24].

References

- [1] Westbrook JH. In: Kear BH, Sims CT, Stoloff NS, Westbrook JH, editors. Ordered alloys: structural applications and physical metallurgy. Baton Rouge, FL: Clair's; 1970. p. 1.
- [2] Westbrook JH. In: Westbrook JH, Fleischer RL, editors. Intermetallic compounds: principles and practice. Chichester: Wiley; 1994. p. 3.
- [3] Shah DM. Scripta Mater 1983;8:997.
- [4] Miner RV, Gabb TP, Gayda J, Hemker KJ. Metall Mater Trans 1986;A17:507.
- [5] Hanriot F, Cailletaud G, Rémy L. In: Freed A, Walker K, editors. High temperature constitutive modelling – theory and application. New York: ASME; 1991. p. 139.
- [6] Sass V. PhD thesis. Berlin: Technischen Universität; 1997.
- [7] Sass V, Feller-Kniepmeier M. Mater Sci Eng 1998;A245:19.
- [8] Siebörger D, Glazel U. Acta Metall 1999;47:397.
- [9] Bettge D, Österle W. Scripta Mater 1999;40:389.
- [10] Wang LN, Liu Y, Yu JJ, Xu Y, Sun XF, Guan HR, et al. Mater Sci Eng 2009;A505:144.
- [11] Carry C, Strudel JL. Acta Metall 1977;25:767.
- [12] Pollock TM, Argon AR. Acta Metall Mater 1992;40:1.
- [13] Westbrook JH. Intermetallic compounds. New York: John Wiley; 1967.
- [14] Cailletaud G. PhD thesis. Ecole des Mines de Paris; 1987.
- [15] Nouailhas D, Cailletaud G. Int J Plast 1995;11:451.
- [16] Fedelich B. Int J Plast 1995;18:1.
- [17] Levkovitch V, Sievert R, Svendson B. Int J Fatigue 2006;28:1791.
- [18] Preussner J, Rudnik Y, Brehm H, Völkl R, Glatzel U. Int J Plast 2008;25:973.
- [19] Österle W, Bettge D, Fedelich B, Klingelhöffer H. Acta Mater 2000;48:689.
- [20] Völkl R, Glatzel U, Feller-Kniepmeier M. Scripta Mater 1994;31:1481.
- [21] Lemarchand C, Devincre B, Kubin LP. J Mech Phys Solids 2001;49:1969.
- [22] Devincre B, Kubin LP, Lemarchand C, Madec R. Mater Sci Eng 2001;309:201.
- [23] Vattré A, Devincre B, Roos A, Feyel F. Eur J Comput Mech, submitted for publication.
- [24] Vattré A, Fedelich B. Int J Plasticity, submitted for publication.
- [25] http://zig.onera.fr/mm_home_page/index.html.
- [26] <http://www.nwnumerics.com/Zebulon/Capabilities.html>.
- [27] Groh S, Devincre B, Kubin LP, Roos A, Feyel F, Chaboche JL. Philos Mag Lett 2003;83:303.
- [28] Groh S, Devincre B, Feyel F, Kubin LP, Roos A, Chaboche JL. In: Shibutani Y, Kitagawa H, editors. Mesoscopic dynamics in fracture process and strength of materials. Dordrecht: Kluwer; 2003. p. 115–235.
- [29] Liu ZL, Liu XM, Zhuang Z, You XC. Int J Plast 2009;25:1436.
- [30] Lemarchand C. PhD thesis. Paris XI: University of Orsay; 1999.
- [31] Devincre B, Roos A, Groh S. In: Finel A et al., editors. Nato sciences series II: mathematics physics and chemistry. Thermodynamics microstructures and plasticity. Dordrecht: Kluwer; 2003. p. 108–275.
- [32] Vattré A, Devincre B, Roos A, Feyel F. In: 9^e colloque national Giens. 2009;1:93. ISBN: 978-2-11-098375-6.
- [33] Madec R, Devincre B, Kubin LP. In: Shibutani Y, Kitagawa H, editors. Mesoscopic dynamics in fracture process and strength of materials. Dordrecht: Kluwer; 2003. p. 115–35.
- [34] Vattré A, Devincre B, Roos A. Intermetallics 2009;17:988.
- [35] Veysière P, Saada G. Dislocations Solids 1997;10:253.
- [36] Fredholm A. PhD thesis. Ecole des Mines de Paris; 1987.
- [37] Saada G, Douin J. Philos Mag 2004;84:807.
- [38] Mura T. Micromechanics of defects in solids. Dordrecht: Kluwer; 1987.
- [39] Royer A, Bastie P, Bellet D, Strudel JL. Philos Mag 1995;72:669.
- [40] Brown LM, Ham RK. In: Kelly A, Nicholson RB, editors. Crystals. Amsterdam: Elsevier; 1971.
- [41] Shah DM, Duhl DN. In: Gall M et al., editors. Superalloys '84. Metals Park (OH): ASM; 1984. p. 105.
- [42] Österle W, Bettge D, Fedelich B, Klingelhöffer H. Acta Mater 1999;48:689.
- [43] Feller-Kniepmeier M, Link T. Mater Sci Eng A 1989;113:191.
- [44] Devincre B, Kubin L, Hoc T. Acta Mater 2006;5:741.
- [45] Kubin L, Devincre B, Hoc T. Acta Mater 2008;20:6040.
- [46] Ashby MF. Philos Mag A 1970;21:399.
- [47] Madec R, Devincre B, Kubin L, Hoc T, Rodney D. Science 2003;301:1879.
- [48] Devincre B, Hoc T, Kubin L. Mater Sci Eng A 2005;400–401:182.

- [49] Kubin L, Canova G, Condat M, Devincre B, Pontikis V, Bréchet Y. Solid State Phen 1992;23–24:455.
- [50] Devincre B, Kubin L, Hoc T. Scripta Mater 2007;57:905.
- [51] Kubin L, Madec R, Devincre B. In: Zbib H, et al., editor. Multiscale phenomena in materials – experiments and modeling related to mechanical behavior, MRS symposium proceedings, vol. 779; 2003, p. 25.
- [52] Devincre B, Hoc T, Kubin LP. Science 2008;320:1745.
- [53] Nye F. Acta Metall 1953;1:153.
- [54] Kubin LP, Devincre B, Hoc T. Philos Mag 2006;86:4023.